

Origin of Coronal Extreme Ultraviolet Shockwaves without a Coronal Mass Ejection Event

Robert Bush^{1,2} · John Stefan² ·
Alexander Kosovichev^{2,3} 

© The author(s) • • •

Abstract

A leading theory of sunquake generation involves flare-accelerated particles depositing energy into the photosphere. Simulations of sunquake excitation suggest co-excitation with wavefronts propagating in the corona and chromosphere, similar to Moreton-Ramsey waves, and large-scale coronal propagating fronts (LCPFs). To investigate observational evidence for the particle-driven mechanism in LCPFs, we compare populations of events associated with and without coronal mass ejections (CMEs). CMEs are known to generate similar EUV shock waves. We employ a visual inspection of flare events that generate LCPFs using Atmospheric Imaging Assembly (AIA) and Large Angle and Spectrometric Coronagraph (LASCO) coronagraph images to find that coronal waves associated with CMEs propagate noticeably faster. Then we examine GOES soft X-ray (SXR) data of “standalone flare events” (those that generate coronal waves without CMEs), focusing on soft X-ray (SXR) characteristics related to magnetic energy release rate. This reveals that such standalone or confined flares differ from sunquake flares: they are less impulsive and energetic than sunquake flares. However, they are more impulsive but less energetic than LCPF-associated flares with a CME. In particular, coronal waves accompanied by CMEs exhibit significantly higher volume emission measures, suggesting a different generation mechanism.

✉ R.N. Bush
robert.bush@tufts.edu

J.T. Stefan
john.stefan@niit.edu

A.G. Kosovichev
alexander.g.kosovichev@njit.edu

¹ Department of Physics and Astronomy, Tufts University, Medford, MA 02155

² Center for Computational Heliophysics, Department of Physics, New Jersey Institute of Technology, Newark, NJ 07102

² NASA Ames Research Center, Moffett Field, Mountain View, CA 94040

Keywords: Coronal Seismology; Flares, Energetic Particles; Waves, Propagation

1. Introduction

Moreton and Ramsey (1960) observed propagating waves in the solar chromosphere using H α images. Later, Uchida (1968) modeled Moreton-Ramsey waves as flare-initiated fast-mode MHD waves propagating in the corona, establishing that coronal shock waves served as the Moreton-Ramsey wave source. These waves are generated when the shock passes below the transition region, generating a chromospheric signature of the large-scale solar coronal shock wave (Patsourakos and Vourlidas 2009). Moreover, these propagating fronts may also be linked to type II radio bursts, radio-wave discharges commonly created when coronal mass ejections (CMEs) accelerate shocks (Nitta et al. 2014). The launch of the Solar and Heliospheric Observatory (SOHO; Domingo, Fleck, and Poland 1995) led to the observation of different types of waves using the Extreme Ultraviolet Telescope (EIT), denoted as the EIT wave (Moses et al. 1997; Thompson et al. 1998). They were initially observed as intensity enhancements in coronal extreme-ultraviolet (EUV) lines, specifically Fe XII line around 195 Å at (approximately greater than) 1.5 MK. The EIT waves have been classified differently due to their strong correlation with CMEs rather than flares (Biesecker et al. 2002; Cliver et al. 2005; Chen 2006). While the nature of EIT waves is not particularly agreed upon, EIT waves are often considered fast-mode MHD waves since their wave fronts are found to be consistent with flare-generated MHD waves going through deceleration (Warmuth et al. 2001, 2004; Vršnak et al. 2006).

Nitta et al. (2013) defined the term "Large-scale Coronal Propagating Fronts," or LCPFs, to refer to EIT-wave-like phenomena, as temporally resolved in Atmospheric Imaging Assembly (AIA; Lemen et al. (2012)) data. LCPFs were cataloged using visual inspection, exhibiting an angular expanse of (approximately greater than) 45 degrees and propagating at least 200 Mm from the center of the eruption. Their study concluded that for many LCPFs, associated CMEs were quite insignificant and that their speeds may depend on external conditions rather than the energy release mechanism.

However, some interest was reopened after 3D acoustic simulations using radially-dependent heating rates derived from the flare radiative hydrodynamic (RADYN) simulations (Allred, Kowalski, and Carlsson 2015) were used to realistically excite (Stefan and Kosovichev 2025, under review) sunquakes. There was evidence of LCPF generation in these global-Sun simulations covering the solar interior, chromosphere, and corona. The flare-excited disturbances propagated from the corona and into the chromosphere, similar to Moreton waves. The generation of coronal waves by proton or electron beams could help explain events where the Moreton waves, and their respective EUV waves, are observed without a CME, particularly for the electron beams that correspond to high-amplitude EUV and Moreton waves but hard-to-detect sunquakes (Stefan and Kosovichev 2025, under review). Sunquakes are helioseismic waves generated

by strong photospheric perturbations during solar flares and were discovered by Kosovichev and Zharkova (1998) using Dopplergrams. These acoustic waves travel through the solar convective zone and are observed after they are refracted upwards, spreading out in the photosphere—often anisotropically—following the impulsive phase of a flare. Recent modeling of sunquakes has suggested that particle beams accelerated by flare energies may be the excitation mechanism responsible for helioseismic events (Sadykov et al. 2024). In a prior study, at least half of the considered events were consistent with the electron beam hypothesis (Stefan and Kosovichev 2020).

X-ray characteristics provide important insight into flare energetics and may reveal the physical processes or mechanisms associated with any helioseismic responses to flares; in turn, this may better inform us as to the origin of mechanisms driving coronal shockwaves not in the presence of a CME, as these mechanisms may be similar to those of sunquakes. Thus, we would initially expect their X-ray characteristics to be similar to flares responsible for helioseismic activity, or at the very least, have different characteristics from flares associated with CME-driven coronal waves. A series of recent studies found that the total magnetic energy released during a solar flare/CME event is partitioned as $51\% \pm 17\%$ for electron acceleration, $17\% \pm 17\%$ for ion acceleration, $7\% \pm 14\%$ for CME kinetic energies, and $7\% \pm 17\%$ for direct heating (Aschwanden et al. 2019). Most of these processes can be observed in soft X-ray (SXR) and extreme ultraviolet (EUV) emission.

We divide this paper into four main sections. Section 1 is the introduction and motivation for this research on coronal waves. Section 2 outlines the methodology for collecting and analyzing the data, using observational and computational methods. Section 3 highlights the results found with histogram and scatterplot visualizations from both the observational methods of AIA and the computational methods from the Geostationary Operational Environmental Satellite (GOES) soft X-ray (SXR) data (Bornmann et al. 1996). Section 4 summarizes our results and draws conclusions based on the data and their implications for future studies.

2. Methodology

2.1. Catalog sourcing

For analysis, we used several catalogs of sunquakes, coronal waves, and CMEs. The sunquakes cataloged are from 2011–2017 in Solar Cycle 24, as outlined by Sharykin and Kosovichev (2020). There are 114 total, identified using at least one of the following three methods: (1) visually inspected in movies showing time sequences of running-differenced Dopplergrams from the Helioseismic and Magnetic Imager (HMI; Scherrer et al. 2012), filtered in a bandwidth of 5–7 mHz, (2) characteristic ridge patterns found in time-distance (TD) diagrams created from photospheric impacts detected in HMI Dopplergrams, or (3) using the helioseismic holography method (Lindsey and Braun 2000), using a Green’s

function of helioseismic waves to calculate egression acoustic power that corresponds to observed Doppler velocities. 94 were found using at least one of the above methods, and an additional 20 were considered potential candidates deduced from the holography method (but not seen in the other two methods).

The coronal wave catalog was sourced from Nitta et al. (2013), which contains Large-scale Coronal Propagating Fronts (LCPFs) observed by the AIA instrument from 2010 to 2022, with ~ 700 events. We specifically examined the standard SolarSoft (Freeland and Handy 1998) movies in AIA's EUV 171 Å and 193 Å channels, made using the running difference method. Visually, the fronts appear in AIA as approximately radial, expanding ripples originating from the flare site, which is seen as a bright flash. LCPFs are defined as events having an angular expanse of $\gtrsim 45^\circ$ and that propagate at least 200 Mm away from the center of the associated eruption. It should be noted that the speeds of these wavefronts are calculated only from 2010 to 2013 (171 events). This speed estimation was accomplished by fitting a first order polynomial to the front edge of the most prominent ridge in the TD plot; there are 24 TD plots, with the eruption center of each event identified as a pole, and the fits from each of the 24 equally spaced 15° -wide sectors are averaged with an assumed uniform uncertainty of 5 Mm in locating the front using MPFIT (Markwardt 2009).

The CME catalog, containing all CMEs manually identified since 1996, was sourced from the Large Angle and Spectrometric Coronagraph (LASCO; Brueckner et al. 1995) onboard SOHO. This CME catalog is generated and maintained at the CDAW Data Center by NASA and The Catholic University of America in cooperation with the Naval Research Laboratory. We mainly looked at two aspects of relevant CMEs: linear speed and mass. The linear speed is found by fitting a straight line to the height-time measurements and serves as an average speed within the LASCO FOV. The mass estimates, while very uncertain, have a representative value that remains quasi-constant after traveling the first several solar radii; if the CME fades within this distance, the mass measured at the last time is used. Computationally, these mass values are found using equations from observed Thomson Scattering of white light from the outer edge of the CME plasma (Gopalswamy et al. 2024).

2.2. Observational methods

We first visually inspected each of the 171 coronal wave events from April 2010 – January 2013 to detect whether or not each one had a CME, and what was the recorded wave speed of that front. Before visual inspection, we cross-referenced the coronal wave catalog with the LASCO CME database, considering any coronal wave event to have a corresponding CME if there was a recorded CME less than 90 minutes from the recorded start time of the coronal wave event. This was to provide time for the CME to be properly observed on the coronagraph, since its effects may not be immediately seen after the flare and/or CME. The population of coronal waves from Nitta et al. (2013) propagate out from an origin, initially looking akin to "dropping a pebble in a pond." As they expand, the fronts become increasingly asymmetric (i.e., they do not solely expand radially), where the fronts in some sectors appear darker or brighter, as well as faster or

slower, as they cross the solar disk. Then, a visual inspection of both coronagraph and 171Å/193Å AIA movies during each recorded wave event was performed. The following event was considered to have an accompanying CME if there was a noticeable plasma ejection traveling beyond the solar limb in the same region of both the coronagraph and 171Å/193Å movies. Additionally, we also recorded the wave speeds as seen in the LCPF catalog, as well as the recorded closest CME time, mass, kinetic energy, speed, and other remarks (such as if an event was poor, only in C2, or a partial halo was observed) as seen in the LASCO catalog. Other notes were recorded regarding the visual strength and size of an observed CME, especially if it was rather weak, faint, and difficult to observe, or if it was quite noticeable. The motivation for this visual inspection stems from the fact that, as stated by the SOHO LASCO CME catalog team, "in the absence of a perfect automatic CME detector program, the manual identification is still the best way to identify CMEs." This was mainly in an effort to confirm our initial tagging of CME-related events, in which coronal wave/LCPF events were only considered to have a corresponding CME event if the start time of the wave (which corresponds to the closest flare start time) was within 90 minutes of the recorded first C2 appearance of a CME in LASCO. Then, we changed events when necessary to either having a CME (yes), not having a CME (no), or being inconclusive (maybe).

2.3. Computational methods

2.3.1. Raw GOES SXR flux data

Next, we looked at the relationship between coronal wave events (both accompanied and not accompanied by a CME) and corresponding flare characteristics derived from the soft X-ray (SXR) data obtained from the GOES satellites. Additionally, we compared the soft X-ray characteristics of the flare populations for CME-less coronal waves with the population associated with sunquakes and their acoustic energy as presented in Sharykin and Kosovichev (2020), and general flares not associated with coronal waves or sunquakes. Flares greater than C1.0 GOES class were considered from 2010–2022; this is the range of available AIA movies of coronal waves/LCPFs maintained through 2024 by the authors of the LCPF study Nitta et al. (2013)¹.

We paid the most attention to flare X-ray characteristics and their relation to energy release rate, as it was previously found that flares that are more impulsive are also more helioseismic (Sharykin and Kosovichev 2020). The first was the impulsive phase duration of each flare, defined as the time interval when the SXR flux was higher than $\max(f_{1-8\text{ \AA}}/10)$, where $f_{1-8\text{ \AA}}$ is the GOES SXR flux in the 1–8 Å channel. The second was the characteristic energy release time estimated from the maximum value of the SXR flux in the 1–8 Å channel divided by the time-derivative of the soft flux, i.e. the maximum value of $f_{1-8\text{ \AA}}/(df_{1-8\text{ \AA}}/dt)$. This quantity relates to how quickly or slowly the SXR emission reaches its peak

¹The LCPF catalog is publicly available at http://aia.lmsal.com/AIA_Waves/index.html

value when energy release is most efficient. Next, we examined the maximum value of the SXR-flux time derivative during the flare event. Lastly, we considered the maximum absolute value of the SXR flux as recorded by GOES.

2.3.2. Conversion of flux ratios to derive flare temperatures and emission measures

Furthermore, we also considered the important characteristics of flare temperature and emission measure. Most of the calculations were performed using code from the Python `sunpy` package (The SunPy Community et al. 2020). The algorithm follows the methodology introduced by Thomas, Starr, and Crannell (1985), which we briefly outline here. The methodology allows us to estimate the temperature, T , and volume emission measure $EM = N_e N_H V$, where N_e is the electron density, N_H the proton density, and V the homogeneous and isothermal source volume, from the reported X-ray fluxes B_4 (0.5 – 4Å channel) and B_8 (1 – 8Å channel). The ratio of the two channels, $R = \frac{B_4}{B_8}$, can be inverted to determine temperature because it is a monotonic function in the 1 – 100 MK range. Once the temperature is known, the emission measure is derived from the longwave 1 – 8Å channel using a temperature-dependent scaling factor. The scaling between R and T , as well as $B_8(T)$ and EM , is found by calculating GOES XRS responses in the two channels. To determine the temperature response of the reported GOES XRS fluxes, Thomas, Starr, and Crannell (1985) consider the measured X-ray flux values B_i , to depend on temperature and volume emission measure as

$$B_i = EM \int_0^{\infty} G_i(\lambda) f(T, \lambda) d\lambda / \overline{G_i}, \quad (1)$$

where $G_i(\lambda)$ is a wavelength-dependent transfer function, EM is volume emission measure, $f(T, \lambda)$ is the isothermal emission spectra and $\overline{G_i}$ is the wavelength-averaged transfer function. The transfer functions for each of the GOES detectors can be found through the data available at the National Geophysical Data Center and/or the Solar Data Analysis Center, derived from the comprehensive calculations performed by Garcia (1994).

While variations in the coefficients of \overline{G} influence the calculated temperature, we should note that only the derived temperatures and emission measures depend on the models used for X-ray spectra from hot plasma. The measured currents in the ion chambers of GOES remain consistent, as these are the raw measured quantities. Then, White, Thomas, and Schwartz (2005) convolves this with models of the X-ray spectrum of an isothermal plasma from the CHIANTI package (Landi et al. 1999; Landi, Feldman, and Dere 2002). Ionization equilibrium is determined using calculations from Mazzotta et al. (1998), which are then implemented in CHIANTI. Continuum from free-free, free-bound and two-photon processes is included (Landi et al. 1999), and we can calculate spectra for logarithmically spaced wavelength bins using both solar photospheric and solar coronal abundances in CHIANTI. These expressions for temperature and emission measure strongly depend on the assumed abundances, especially at higher temperatures. This is where the free-bound emission processes make the

continuum dominate the Sun’s X-ray spectrum (White, Thomas, and Schwartz 2005). Using the derived polynomial approximations from Thomas, Starr, and Crannell (1985), the temperature is obtained from

$$T(R) = A(0) + A(1)R + A(2)R^2 + A(3)R^3 \quad (2)$$

and once the temperature is known, the emission measure is derived from $EM = 10^{55} B_8/b_8(T) \text{ cm}^{-3}$, where B_8 is the $1 - 8\text{\AA}$ flux in the standard GOES unit of W m^{-2} and

$$b_8(T) = B(0) + B(1)T + B(2)T^2 + B(3)T^3 \quad (3)$$

is the normalized response. White, Thomas, and Schwartz (2005) (and the `sunpy` code) derives the polynomial approximations for all GOES satellites using CHIANTI spectral models, which then gives us the flare temperature and the total amount of hot plasma in the flare regions (i.e., the emission measure) of the flare events.

3. Results

First, we separate the distribution of LCPF propagation speeds based on the presence or absence of an accompanying CME (**Figure 1**). Colors in **Figure 1** highlight three different populations of coronal wave events: coronal waves with a CME (blue), coronal waves without a CME (red) and coronal waves that were difficult to identify whether or not they have a CME (orange). Since all coronal wave events correlate with flare events, we applied a log-normal fit to each histogram distribution (Aoki, Yashiro, and Shibata 2004; Verbeeck et al. 2019). The mean, median, and standard deviation, with uncertainties found using the standard error propagation formula, are found in **Table 1** of the Appendix. If the continuous random variable X is log-normally distributed, then $Y = \ln(X)$ has a normal distribution. If μ and σ are the mean and standard deviation of Y , then $X = \exp(\mu + \sigma Z)$, where Z is a standard normal variable. The lognormal distribution also has mean $\exp(\mu + \frac{\sigma^2}{2})$, median $\exp(\mu)$, and variance $[\exp(\sigma^2) - 1] \exp(2\mu + \sigma^2)$ (Crow and Shimizu 1988).

We observed that the coronal propagating front events had differing median propagation speeds, where those that had an accompanying CME traveling with median speed $698.75 \pm 28.22 \text{ km/s}$, those that did not have an accompanying CME traveling with median speed $504.15 \pm 18.96 \text{ km/s}$, and events where a visual inspection could not conclude the presence of a CME whose LCPF propagates with median speed $572.32 \pm 31.56 \text{ km/s}$. From these distributions, we see that coronal waves without a CME are significantly slower and more concentrated between $300 - 700 \text{ km/s}$, while the coronal waves with a CME are much more distributed across the axis, supported by its large standard deviation of $323.83 \pm 44.71 \text{ km/s}$. Then, we analyzed the correlation of the coronal wave events associated with a CME to that respective CME’s linear mass and speed (**Figure 2**). We find only a weak correlation between coronal wave speed and

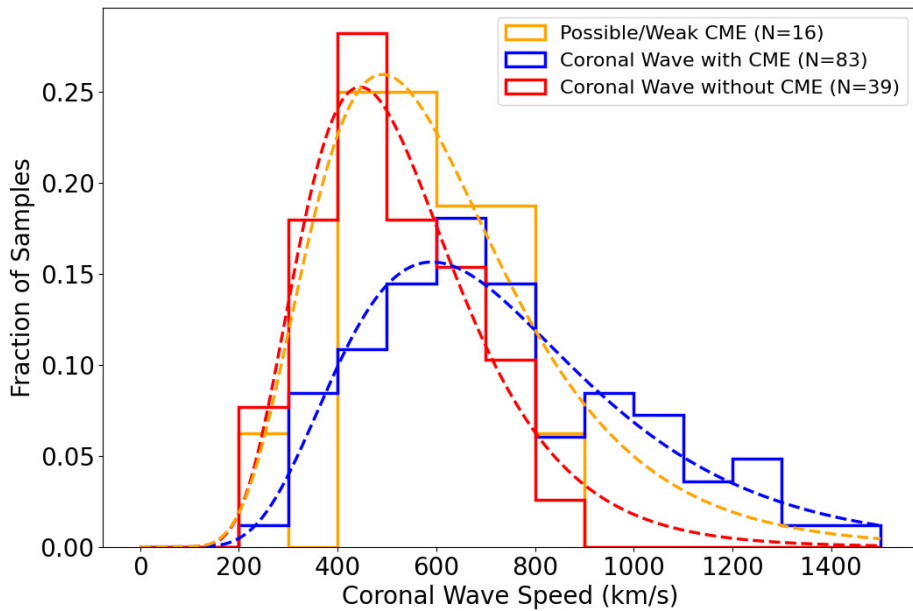


Figure 1. A histogram showing 171 EUV wave events (2010-2013) from the Nitta LCPF AIA movie catalog that were cross-referenced with the LASCO CME Catalog and observed for the presence of a CME using a combination of AIA and coronagraph data in 193 angstroms. The y-axis gives the total number of EUV events in the catalog and the x-axis highlights EUV wave speeds. The distribution in red includes EUV wave events that were not followed by a CME, the distribution in blue includes EUV wave events that were noticeably followed by a CME, and the orange distribution includes indeterminate events. The dashed lines indicate the corresponding log-normal distributions from the observed mean and standard deviation.

CME mass, and an even weaker (though skewed) dependence on CME speed. The linear regression lines are very weak, and the Spearman correlation coefficients are 0.02 and 0.07 respectively.

Flare X-ray properties from the GOES data provide the most important parameters of the flare energetics, meaning the statistical comparison of the X-ray and helioseismic energetics is an important step to understanding the physical processes associated with the helioseismic response. We first compare the population of flares with CME-less coronal waves to the populations of sunquakes (**Figure 3**), as a potential co-excitation of coronal waves and sunquakes were the original motivation of this study. Colors in **Figure 3** highlight two populations of flare events: flares with coronal waves that did not have an accompanying CME and were not associated with a sunquake (blue), and flares with an associated sunquake (red). The sunquake distribution is qualitatively similar to the one derived in Sharykin and Kosovichev (2020) for the sunquake events of Solar Cycle 24 – overall, flares associated with sunquakes are highly impulsive events. Their impulsive and characteristic energy release time exhibit strongly left-skewed distributions, indicating shorter time durations. Moreover, these flares vary between GOES classes M and X, and generally display higher

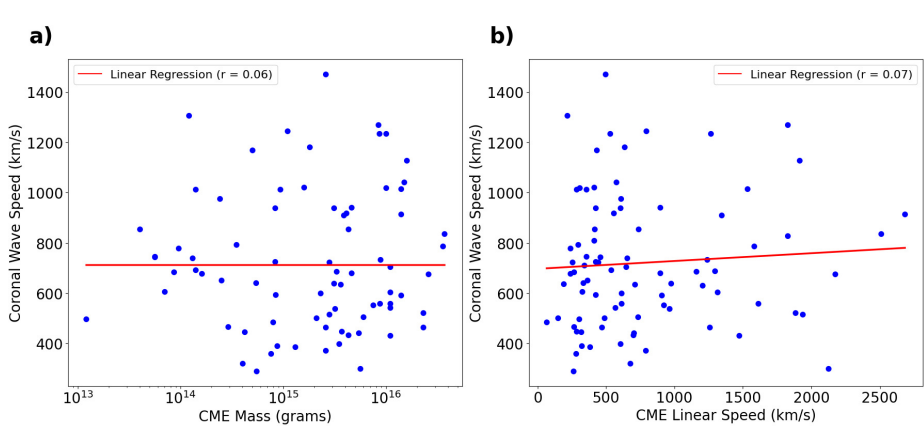


Figure 2. (a) is a scatter plot of CME mass versus coronal wave speeds, and (b) is CME linear speed versus coronal wave speeds. The data on the x-axis was obtained via the LASCO CME catalog, while the y-axis are the 2010-2013 dates from Nitta et. al 2013.

maximum values of the SXR flux time derivative, signifying powerful, energetic flares that rapidly release energy..

However, there are some slight differences from the distribution in Sharykin and Kosovichev (2020). This may be for a few reasons, most notably choices of binning, limits on the axes, and that, for purposes of this paper, we considered all 114 cataloged events as sunquakes (regardless of whether they were considered “sunquake candidate” due to their weak acoustic signals). The mean, median and standard deviation, with uncertainties found using the standard error propagation formula, are found in **Table 2** for the impulsive phase, **Table 3** for the characteristic energy release rate, **Table 4** for the maximum value of the SXR flux time derivative, and **Table 5** for the SXR flux/GOES class. Panel (d) revealed that isolated coronal waves have a lower maximum SXR flux that varies between the high C and low M flare classes, spread out less than the sunquake distribution. Moreover, we see in Panel (a) that flares with isolated coronal waves are much less impulsive, and can span from a few minutes to almost one hundred minutes. This is supported by the characteristic energy-release time in Panel (b), which shows a smaller, less pronounced peak but still has a much wider variation. This difference is more pronounced in terms of the maximum values of the SXR flux time derivative in Panel (c), where both distributions have smaller standard deviations and noticeable peaks, showing that the isolated coronal wave flares have an order of magnitude lower max SXR flux time derivative than that of sunquakes.

Then we compared flares in the 2010-2022 time frame that were not associated with a sunquake or coronal wave with the population of CME-less coronal wave flares previously described (**Figure 4**). Colors in **Figure 4** highlight two populations of flare events: flares with coronal waves that did not have an accompanying CME and were not associated with a sunquake (blue), and flares that were not associated with any type of coronal wave or sunquake (green). Note that **Tables 2, 3, 4 and 5** also have the mean, median, and standard deviations of these distributions as well. Panel (a) shows that isolated coronal wave events

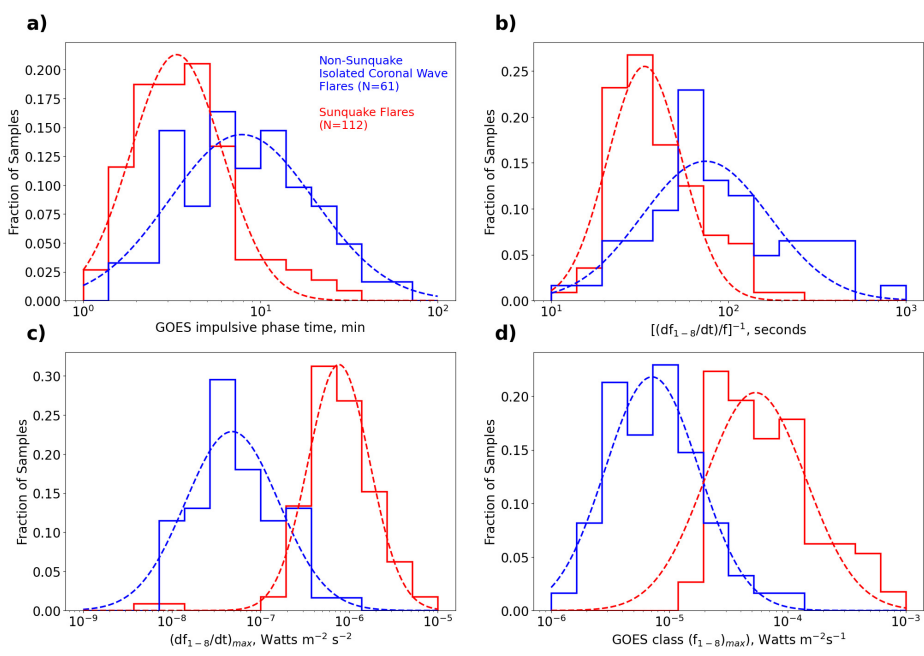


Figure 3. These four histograms compare certain flares of C1.0 or greater from 2010-2022, with the dotted line being the median for distribution. The red highlights flares that were associated with sunquakes as outlined in Sharykin and Kosovichev (2020), while those in blue are coronal wave flares (without a CME or filament eruption) recorded in Nitta et al. (2013). (a) is the impulsive phase duration, (b) is the characteristic energy release time estimated as the maximum value of $f_{1-8}/(df_{1-8}/dt)$, (c) is the maximum value of the SXR flux time derivative, and (d) is the SXR flux.

(without sunquakes) have marginally higher impulsive phase durations than events without any photospheric or coronal seismic events. However, panel (b) indicates flares with isolated coronal waves still have a shorter characteristic growth time, and panel (c) presents a slightly higher peak in the max SXR flux time derivative of the isolated coronal wave events to show higher energy release rates. Panel (d) shows that these events also have a consistently higher GOES flare class, meaning greater radiation (and thus higher energy) than a flare with no sunquake or coronal wave.

Finally, we compare the same population of CME-less coronal wave flares with the rest of the coronal wave population that was related to a CME (**Figure 5**). Coronal waves associated with CMEs are well explained by the CME model, which cites EUV Imaging Telescope (EIT) waves as strongly tied to CMEs through stretching of closed field lines (Ballai, Erdélyi, and Pintér 2005). Colors in **Figure 5** highlight two populations of flare events: flares with coronal waves that did not have an accompanying CME and were not associated with a sunquake (blue), and flares with coronal waves that did accompany a CME and were not associated with a sunquake (purple). Again, **Tables 2, 3, 4** and **5** also have the mean, median, and standard deviations of these distributions.

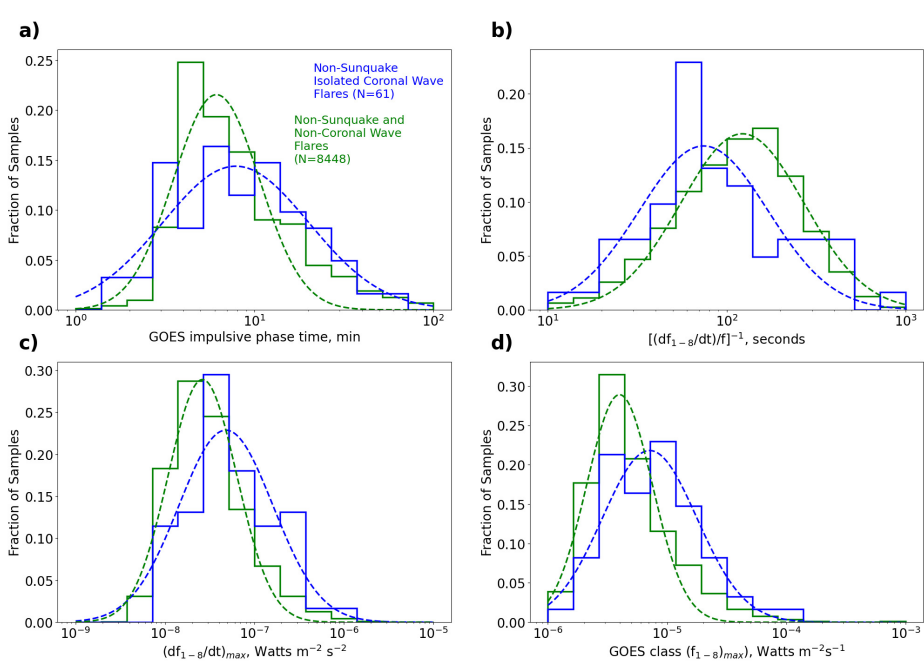


Figure 4. Those in blue are the same as in **Figure 3**, and the green are all other flares that were not related to either sunquakes or coronal waves.

Overall, the CME-related distributions are much wider than the sunquake flares, non-coronal wave and non-sunquake flares, and isolated coronal wave flares, as given by the comparatively high standard deviation for Panels (a), (b), (c), and (d). For example, in panel (b), isolated coronal wave flare events have a standard deviation of 209.49 ± 126.35 seconds compared to CME-related coronal wave flare events having a standard deviation of 697.70 ± 264.73 seconds. Likewise in panel (d), isolated coronal wave flare events have a standard deviation of $2.85 \times 10^{-5} \pm 1.28 \times 10^{-5}$ Watts $m^{-2}s^{-1}$ while CME-related coronal wave events have a greater standard deviation of $3.12 \times 10^{-3} \pm 3.12 \times 10^{-3}$ Watts $m^{-2}s^{-1}$. Panel (a) demonstrates that isolated coronal wave flares have a shorter impulsive phase duration, meaning they are more impulsive and have faster energy release than flares that have CME-related coronal waves. Panel (b) supports this conclusion, as the distribution of the CME-related coronal wave flares is shifted and has a much smaller peak. However, panel (c), the maximum value of the SXR flux time-derivative—which characterizes the maximal energy release rate—shows the two populations having similar distributions. Nevertheless, the isolated coronal wave flares' median is slightly lower than the CME-related coronal wave flares with a more pronounced peak in the distribution. Panel (d) presents CME-related coronal wave flares' GOES class as ranging from high C to X, with a median a bit above that of isolated coronal wave flares and most concentrated in the middle M class. Altogether, this reveals that while isolated coronal wave flares may have faster energy release, they release overall less energy than flares that are associated with a CME.

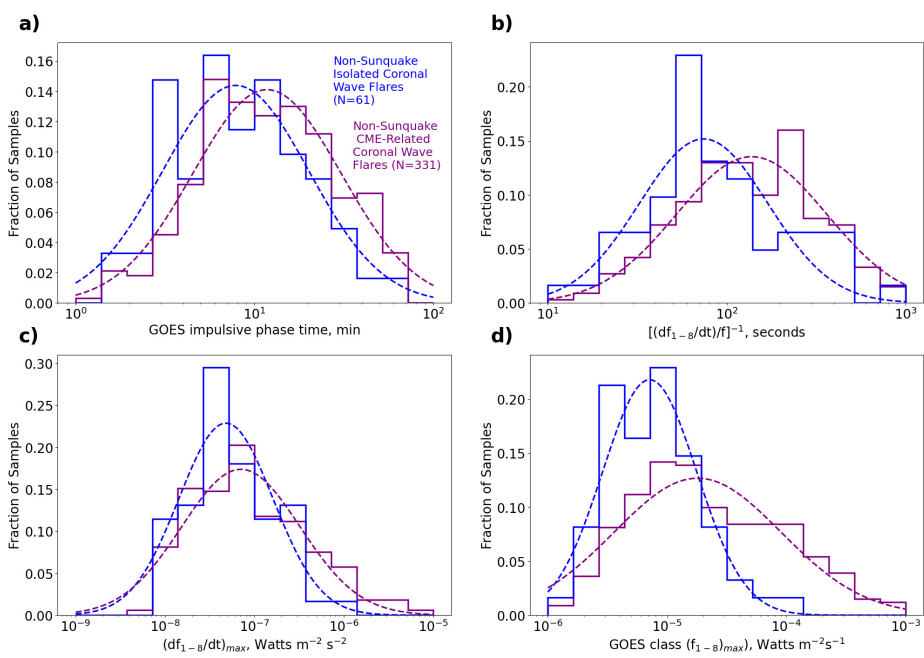


Figure 5. Those in blue are the same as in **Figure 3**, and the purple are flares that do not have a sunquake, but are coronal waves that have an accompanying CME.

Figure 6 presents distributions of the maximum volume emission measure and maximum temperature for each flare to illustrate further differences in magnetic energy release between the populations of CME-related and isolated coronal wave flares. The emission measure provides information about the density and volume of the hot plasma, and larger values (between 10^{46} and 10^{50} cm $^{-3}$) are characteristic of stronger flares with more substantial heating. When coupled with higher peak temperatures, these enhanced emission measures indicate a greater release of magnetic energy (Feldman et al. 1996). The temperature and emission measure of the flare events are computed using the GOES SXR flux as described in Section 2.3.2. Colors in **Figure 6** highlight three populations of flare events (where sunquakes may be found in any of the three populations): flares with coronal waves that did not have an accompanying CME (red), flares with coronal waves that did accompany a CME (blue), and flare events without any coronal wave event (green). Moreover, the mean, median and standard deviations of these distributions for the maximum emission measure histograms can also be found in **Table 6** using photospheric abundances and **Table 7** using coronal abundances. The same statistics are available for the flare temperatures in **Table 8** using photospheric abundance and **Table 9** using coronal abundance.

Panels (a1) and (a2) show the maximum flare emission measure and temperature using photospheric abundance, while panels (b1) and (b2) use coronal abundance. The main difference between the two appears only to be a scaling factor, likely from FIP-related (first ionization potential effect) differences in the

abundances; elements with FIPs of less than 10 eV have abundances three to four times greater in the corona than in the photosphere (Doschek et al. 2018). However, this difference is more pronounced in the emission measure, where cooler flares (~ 15 MK) have comparable values for the max flare temperature in both photospheric and coronal abundances; however, for hotter flares (~ 35 MK), coronal abundance leads to nearly 25% lower derived temperatures (White, Thomas, and Schwartz 2005).

Panels (a2) and (b2) show that CME-related coronal wave flares are the hottest, followed by isolated coronal wave flares and then by the other non-coronal wave flares. The non-coronal wave flare population peaks (especially in photospheric abundance) around 10 MK and has the most narrow distribution of the three populations. The widest distribution is the CME-related flare population, which does not have a clear maximum in the observed distribution in either abundance and is shifted to the right, signifying higher temperatures. The isolated coronal wave flare distribution has a clear peak in the coronal abundance that is higher than that of the non-coronal wave events, but is shifted to the left of the CME-related events. Note that the uncertainties are more pronounced in **Tables 8** and **9**. In other words, CME-related coronal wave flares have a more significant release of magnetic energy than isolated coronal wave flares because a higher temperature means more energy was released and converted into heat.

Panels (a1) and (b1) present a significant difference in the emission measure of coronal wave flares with and without a CME. Isolated coronal wave flares have the lowest emission measure and seem to fall in the same range as a general flare without any coronal wave event, while coronal wave events with a CME have significantly greater emission measure. It appears that this characteristic reveals a stark difference between the isolated coronal wave flares (median EM $6.69 \times 10^{48} \pm 0.823 \times 10^{48} \text{ cm}^{-3}$) and CME-related coronal wave flares (median EM $69.2 \times 10^{48} \pm 15.9 \times 10^{48} \text{ cm}^{-3}$); these numerical values are summarized in **Table 7**. The broader distribution of CME-related coronal wave flares indicates a greater amount of hot, dense plasma, a key indicator of a more substantial and energetic flare event involving a significant amount of heated material that emits intense SXR radiation. This is supported by the nature of CMEs, which are ejections of large, dense volumes of hot plasma into the heliosphere.

We also investigated the correlation of the coronal wave speeds with both max flare emission measure and max flare temperature (using both coronal and photospheric abundances) to determine whether either of these factors influences the coronal wave speeds (**Figure 7**). Panels (a1) and (b1) show (with some outliers) that isolated coronal wave flares between 2010 and 2013 are generally slower and have a smaller emission measure than CME-related coronal wave flares, which also have a weak linear correlation between wave speed and emission measure. Panels (a2) and (b2) demonstrate that the slower isolated coronal wave flares are also cooler, and have an even weaker linear correlation between wave speed and temperature, as the temperature and speeds of CME-related coronal wave flares are much more sparsely populated. The dark, bright, or unclear fronts for each of these coronal wave events were observed by eye for each event recorded in Nitta et al. (2013) in 171Å. The small sample of isolated flares mostly have unclear or dark fronts, which seems to agree with both **Figure 6** and panels

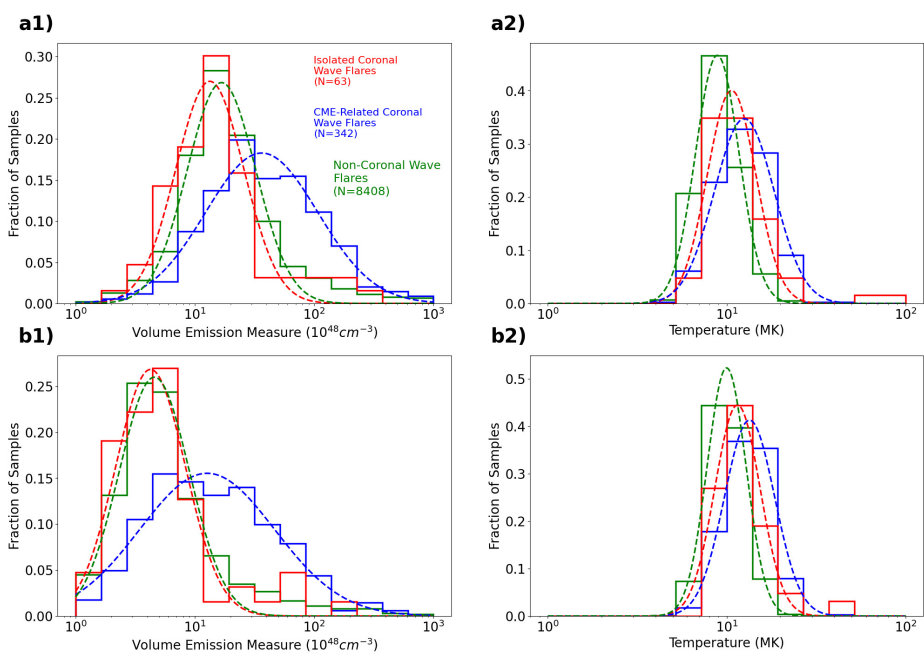


Figure 6. Histograms of emission measure + flare temperature, with (a1) and (a2) corresponding to photospheric abundance, and (a2) and (b2) corresponding to coronal abundance, using code inspired by calculations from White, Thomas, and Schwartz (2005). Note that sunquake-active flares are excluded here. The red distributions correspond to any coronal wave flare not accompanied by a CME, blue to flares with coronal waves that most likely have a CME, and those in green are the rest of the C1.0+ flares not considered in the other two categories. LCPFs observed as having a bright propagating front in 171 Å are denoted with a square symbol, those with a dark front with a triangle, and those with an unclear front with a circle.

(a2) and (b2) of **Figure 7** in that these isolated wave events may be slower and cooler, thus having less energy. The emission measure versus wave speed seems to be slightly more correlated with wave speed than the temperature, with (a1) and (b1) having Spearman correlation coefficients of 0.43 and 0.42 respectively, while (a2) and (b2) have correlation coefficients of 0.26 and 0.27 respectively.

4. Discussion and Conclusion

We have performed a comprehensive study on solar flares from 2010-2022 that are correlated to coronal waves (or large-scale coronal propagating fronts) to understand how they may be affected by the presence of a coronal mass ejection. We analyze GOES SXR emission and its temporal evolution for coronal-wave-associated flares, comparing events with accompanying CMEs to those without. The analysis further distinguishes non-sunquake isolated coronal wave flares from flares associated with sunquakes and from flares exhibiting neither a sunquake nor a coronal wave. By cross-referencing catalogs of sunquakes, CMEs, and

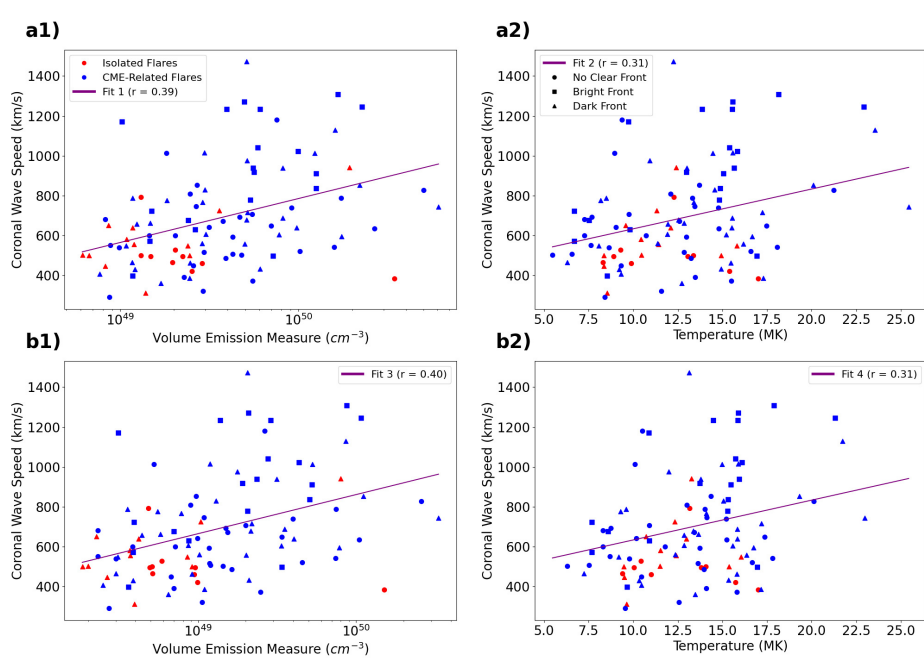


Figure 7. (a1) and (b1) are scatter plots of emission measure versus coronal wave speeds, corresponding to photospheric and coronal abundances respectively. (a2) and (b2) are flare temperatures versus coronal wave speeds corresponding to photospheric and coronal abundances respectively. The data on the x-axis was calculated using the same code mentioned in **Figure 6**, and the y-axis are the 2010-2013 events from Nitta et al. (2013).

coronal waves, we statistically compare these flare populations. The main results can be summarized as follows:

- i) We found that coronal waves without an observed coronal mass ejection moved more slowly than coronal waves with a coronal mass ejection. Our fitting analysis has shown that coronal waves without CMEs are concentrated at lower propagation speeds with a clear maximum in the observed distribution, whereas coronal waves with CMEs span a much broader speed distribution that is skewed towards higher propagation speeds. Note that these wave speeds are originally from Nitta et al. (2013) and include only dates from 2010 to 2013.
- ii) Our analysis also revealed that flares associated with CME-less coronal waves release their magnetic energy faster (i.e. more impulsive) than CME-related coronal wave flares; however, it seems CME-related coronal wave flares have more energy, seen in their greater maximum value of the soft X-ray time derivative and X-ray class.
- iii) It was supported that CME-related flares have more energy in their significantly higher maximum flare emission measure and slightly hotter maximum flare temperature compared to CME-less coronal wave flares. Moreover, there is a weak but apparent correlation between coronal wave speed and emission measure or temperature.

In our initial investigation, we examined whether seismically active (producing sunquakes) flares can also generate coronal shockwaves from flare-accelerated particles. We looked for similarities in the distributions of sunquake and CME-less coronal wave flare events with the temporal characteristics of the flare soft X-ray emission. Although the results are not conclusive in answering the exact mechanism that generates either the flare's helioseismic response or coronal shock waves without a CME burst, it does support the conclusion that coronal waves without an accompanying CME are driven by a process distinct from EUV Imaging Telescope (EIT) waves and CME model scenarios.

The catalog from Nitta et al. (2013) contained only large-scale coronal propagating front speeds from 2010-2013, so further studies using speeds beyond 2013 with the time-distance method would allow us to draw better conclusions from the results. Additionally, as mentioned in Sharykin and Kosovichev (2020), a further detailed multi-spectral study considering characteristics of the magnetic field structure and flare emission in other ranges of the electromagnetic spectrum would be promising, particularly in radio imaging. Type III radio bursts are related to fast electron beams moving upward and escaping the corona by traveling along magnetic field lines at near-relativistic speeds, exciting plasma emission that generates radio waves (Reid and Ratcliffe 2014). The Expanded Owens Valley Solar Array (Gary et al. 2018) observes in the microwave regime (1-18 GHz) with temporal resolution of about 1s at more than 100 frequency channels; moreover, they also provide solar spectral-imaging observations in high resolution, meaning it is quite easy to find the source region and the relationship between the burst and the magnetic field in that region (Tan et al. 2023). This can shed more light on what characteristics of flares, both in the pre-flare atmosphere and the flare dynamics, affect how energy is redistributed throughout the solar atmosphere.

This study advances in understanding the distribution of flare energy and the effect flare-accelerated particles have on eruption events, which may be used for new opportunities to constrain models of sunquake, flare, and coronal shock wave excitation. It will contribute to a better understanding of the mechanisms of sunquakes, flares, Moreton-Ramsey waves, and large-scale coronal propagating fronts. Overall, we find evidence for the generation of coronal waves without a CME. The substantially lower volume emission measure is a strong indicator distinguishing coronal wave events with or without associated CMEs. Isolated coronal wave events are more impulsive (although weaker) than populations without coronal waves or CME-related coronal waves. While the distributions of isolated flare properties differ from those of helioseismic events, the two populations share the important characteristic of rapid energy release. Finding further evidence of flare-accelerated particles' effect on the corona will allow for a unification of coronal seismology in the outer atmosphere with helioseismology and the generation of acoustic waves in the Sun's interior. Moreover, it enables a more comprehensive characterization of solar flares, which helps science teams more accurately predict space weather.

Appendix

The following tables show the calculated median, mean and standard deviation (with uncertainties found by error propagation) for the log-normal curve fits of the plots in each figure. Note that the tables are separated by the certain characteristic of the flare/coronal wave they highlight (i.e., coronal wave speeds, impulsive phase duration, emission measure). Moreover, coronal and photospheric abundances are divided into separate tables.

Table 1. Statistics of coronal wave speeds, in km s^{-1} , for different CME associations.

Category	Median	Mean	Std. Dev.
Coronal wave without CME	504.15 ± 18.96	536.16 ± 23.81	194.08 ± 27.60
Coronal wave with CME	698.75 ± 28.22	759.60 ± 37.17	323.83 ± 44.71
Possible/weak CME	572.32 ± 31.56	617.87 ± 40.25	251.37 ± 47.39

Table 2. Statistics of the impulsive phase duration in minutes for different flare populations.

Category	Median	Mean	Std. Dev.
Isolated coronal wave	19.07 ± 5.05	29.72 ± 11.22	35.52 ± 20.54
Sunquake	4.79 ± 0.33	5.72 ± 0.53	3.72 ± 0.67
No sunquake or coronal wave	8.33 ± 0.86	9.71 ± 1.30	5.82 ± 1.57
CME-related coronal wave	29.29 ± 4.57	46.24 ± 10.15	56.51 ± 18.65

Table 3. Statistics of the characteristic energy release time, $[df_{1-8}/dt/f]^{-1}$ in seconds for different flare populations.

Category	Median	Mean	Std. Dev.
Isolated coronal wave	147.21 ± 40.81	207.28 ± 79.74	205.49 ± 126.35
Sunquake	42.47 ± 3.97	47.71 ± 5.66	24.43 ± 6.44
No sunquake or coronal wave	229.37 ± 12.81	314.11 ± 24.15	293.88 ± 36.77
CME-related coronal wave	351.09 ± 63.09	560.56 ± 141.99	697.70 ± 264.73

Table 4. Statistics of the maximum time derivative of the GOES SXR flux, $(df_{1-8}/dt)_{\max}$ in $10^{-6}Wm^{-2}s^{-2}$ for different flare populations.

Category	Median	Mean	Std. Dev.
Isolated coronal wave	0.209 ± 0.124	0.436 ± 0.383	0.798 ± 1.000
Sunquake	1.450 ± 0.138	2.000 ± 0.261	1.890 ± 0.401
No sunquake or coronal wave	0.0571 ± 0.00537	0.0842 ± 0.0110	0.0914 ± 0.0186
CME-related coronal wave	0.717 ± 0.350	2.290 ± 1.650	6.950 ± 6.790

Table 5. Statistics of the max GOES SXR flux, $(f_{1-8})_{\max}$ in $10^{-5}Wm^{-2}s^{-1}$ for different flare populations.

Category	Median	Mean	Std. Dev.
Isolated coronal wave	1.64 ± 0.341	2.49 ± 0.729	2.85 ± 1.28
Sunquake	14 ± 5.87	22.8 ± 13.9	29 ± 27
No sunquake or coronal wave	0.595 ± 0.0491	0.726 ± 0.0801	0.509 ± 0.104
CME-related coronal wave	24.2 ± 12.1	88.4 ± 65.3	312 ± 312

Table 6. Statistics of the max volume emission measure (photospheric abundance) in $10^{48}cm^{-3}$ for different flare populations.

Category	Median	Mean	Std. Dev.
Isolated coronal wave	20.5 ± 2.36	25.5 ± 3.91	18.7 ± 5.16
CME-related coronal wave	117 ± 17.2	211 ± 44.1	315 ± 95.2
Non-coronal wave	25.9 ± 1.44	32.1 ± 2.40	23.7 ± 3.18

Table 7. Statistics of the max volume emission measure (coronal abundance) in $10^{48}cm^{-3}$ for different flare populations.

Category	Median	Mean	Std. Dev.
Isolated coronal wave	6.69 ± 0.823	8.38 ± 1.40	6.35 ± 1.89
CME-related coronal wave	69.2 ± 15.9	162 ± 54.1	342 ± 159
Non-coronal wave	7.23 ± 0.44	9.09 ± 0.747	6.93 ± 1.01

Table 8. Statistics of the max flare temperature (photospheric abundance) in megakelvin (MK) for different flare populations.

Category	Median	Mean	Std. Dev.
Isolated coronal wave	11.73 ± 0.41	12.32 ± 0.51	3.94 ± 0.53
CME-related coronal wave	14.54 ± 0.30	15.67 ± 0.39	6.27 ± 0.42
Non-coronal wave	9.58 ± 0.08	9.96 ± 0.09	2.84 ± 0.09

Table 9. Statistics of the max flare temperature (coronal abundance) in MK for different flare populations.

Category	Median	Mean	Std. Dev.
Isolated coronal wave	12.49 ± 0.30	13.03 ± 0.37	3.87 ± 0.40
CME-related coronal wave	14.90 ± 0.36	15.70 ± 0.44	5.22 ± 0.46
Non-coronal wave	10.62 ± 0.06	10.96 ± 0.07	2.78 ± 0.09

Acknowledgements The observational data are courtesy of the SDO/AIA, GOES, and LASCO science teams. The CME catalog is generated and maintained at the CDAW Data Center by NASA and The Catholic University of America in cooperation with the Naval Research Laboratory. SOHO is a project of international cooperation between ESA and NASA. The LCPF catalog is compiled and maintained using SDO/AIA data by Nariaki V. Nitta at the Lockheed Martin Solar and Astrophysics Laboratory.

Author Contribution R.N. Bush wrote the main manuscript text and prepared figures 1-7 as well as tables 1-9. J.T. Stefan edited the main manuscript and assisted in the data collection and troubleshooting of figures 1, 3, 4, 5, and 6. A.G. Kosovichev edited the main manuscript and provided suggestions on error analysis for figures 1, 3, 4, 5, and 6. All authors reviewed the manuscript.

Funding The work was partially supported by the NSF grant 1916509, and NASA grants 80NSSC22M0162, 80NSSC23K0097, and 80NSSC25K7675.

Data Availability The catalog of Large-scale Coronal Propagating Fronts (LCPFs) is available online at https://aia.lmsal.com/AIA_Waves/index.html, and the original paper reporting the 2010–2013 wave speeds is available at <https://doi.org/10.1088/0004-637X/776/1/58>. The catalog of sunquakes from Solar Cycle 24 is available at <https://solarflare.njit.edu/sunquakes/sunquakes.html>, with the original paper available at <https://doi.org/10.3847/1538-4357/ab88d1>. The SOHO LASCO CME Catalog is available at https://cdaw.gsfc.nasa.gov/CME_list/. The GOES data archive is available at <https://www.ngdc.noaa.gov/stp/satellite/goes/dataaccess.html>, with data analysis performed using SunPy documentation available at https://docs.sunpy.org/en/stable/generated/gallery/time_series/goes_xrs_example.html. Additionally, SunPy documentation describing the calculation of temperature and the corresponding volume emission measure from GOES/XRS data is available at https://docs.sunpy.org/projects/sunkit-instruments/en/stable/api/sunkit_instruments.goess_xrs.calculate_temperature_em.html.

Declarations

Conflict of interest The authors declare no competing interests.

References

Allred, J.C., Kowalski, A.F., Carlsson, M.: 2015, A Unified Computational Model for Solar and Stellar Flares. *Astrophys. J.* **809**, 104. [DOI](#). [ADS](#).

Aoki, S.I., Yashiro, S., Shibata, K.: 2004, The Log-normal Distributions of Physical Quantities of Flare associated Coronal Mass Ejections (CMEs), and Flare/CME Model of Gamma-ray Bursts. *arXiv e-prints*, astro. [DOI](#). [ADS](#).

Aschwanden, M.J., Caspi, A., Cohen, C.M.S., Holman, G., Jing, J., Kretzschmar, M., Kontar, E.P., McTiernan, J.M., Mewaldt, R.A., O'Flannagain, A., Richardson, I.G., Ryan, D., Warren, H.P., Xu, Y.: 2019, Global Energetics of Solar Flares and Coronal Mass Ejections. In: *Journal of Physics Conference Series, Journal of Physics Conference Series* **1332**, 012002. [DOI](#). [ADS](#).

Ballai, I., Erdélyi, R., Pintér, B.: 2005, On the Nature of Coronal EIT Waves. *Astrophys. J. Lett.* **633**, L145. [DOI](#). [ADS](#).

Biesecker, D.A., Myers, D.C., Thompson, B.J., Hammer, D.M., Vourlidas, A.: 2002, Solar Phenomena Associated with "EIT Waves". *Astrophys. J.* **569**, 1009. [DOI](#). [ADS](#).

Bornmann, P.L., Speich, D., Hirman, J., Matheson, L., Grubb, R., Garcia, H., Viereck, R.: 1996, GOES x-ray sensor and its use in predicting solar-terrestrial disturbances. In: Washwell, E.R. (ed.) *GOES-8 and Beyond, Society of Photo-Optical Instrumentation Engineers (SPIE) Conference Series* **2812**, 291. [DOI](#). [ADS](#).

Brueckner, G.E., Howard, R.A., Koomen, M.J., Korendyke, C.M., Michels, D.J., Moses, J.D., Socker, D.G., Dere, K.P., Lamy, P.L., Llebaria, A., Bout, M.V., Schwenn, R., Simnett, G.M., Bedford, D.K., Eyles, C.J.: 1995, The Large Angle Spectroscopic Coronagraph (LASCO). *Sol. Phys.* **162**, 357. [DOI](#). [ADS](#).

Chen, P.F.: 2006, The Relation between EIT Waves and Solar Flares. *Astrophys. J. Lett.* **641**, L153. [DOI](#). [ADS](#).

Cliver, E.W., Laurenza, M., Storini, M., Thompson, B.J.: 2005, On the Origins of Solar EIT Waves. *Astrophys. J.* **631**, 604. [DOI](#). [ADS](#).

Crow, E.L., Shimizu, K.: 1988, *Lognormal Distributions: Theory and Applications*, Dekker, New York.

Domingo, V., Fleck, B., Poland, A.I.: 1995, SOHO: The Solar and Heliospheric Observatory. *Space Sci. Rev.* **72**, 81. [DOI](#). [ADS](#).

Doschek, G.A., Warren, H.P., Harra, L.K., Culhane, J.L., Watanabe, T., Hara, H.: 2018, Photospheric and Coronal Abundances in an X8.3 Class Limb Flare. *Astrophys. J.* **853**, 178. [DOI](#). [ADS](#).

Feldman, U., Doschek, G.A., Behring, W.E., Phillips, K.J.H.: 1996, Electron Temperature, Emission Measure, and X-Ray Flux in A2 to X2 X-Ray Class Solar Flares. *Astrophys. J.* **460**, 1034. [DOI](#). [ADS](#).

Freeland, S.L., Handy, B.N.: 1998, Data Analysis with the SolarSoft System. *Sol. Phys.* **182**, 497. [DOI](#). [ADS](#).

Garcia, H.A.: 1994, Temperature and Emission Measure from Goes Soft X-Ray Measurements. *Sol. Phys.* **154**, 275. [DOI](#). [ADS](#).

Gary, D.E., Chen, B., Dennis, B.R., Fleishman, G.D., Hurford, G.J., Krucker, S., McTiernan, J.M., Nita, G.M., Shih, A.Y., White, S.M., Yu, S.: 2018, Microwave and Hard X-Ray Observations of the 2017 September 10 Solar Limb Flare. *Astrophys. J.* **863**, 83. [DOI](#). [ADS](#).

Gopalswamy, N., Michalek, G., Yashiro, S., Mäkelä, P., Akiyama, S., Xie, H., Vourlidas, A.: 2024, The SOHO LASCO CME Catalog – Version 2. *arXiv e-prints*, arXiv:2407.04165. [DOI](#). [ADS](#).

Kosovichev, A.G., Zharkova, V.V.: 1998, X-ray flare sparks quake inside Sun. *Nature* **393**, 317. [DOI](#). [ADS](#).

Landi, E., Feldman, U., Dere, K.P.: 2002, CHIANTI-An Atomic Database for Emission Lines. V. Comparison with an Isothermal Spectrum Observed with SUMER. *Astrophys. J. Suppl. Ser.* **139**, 281. [DOI](#). [ADS](#).

Landi, E., Landini, M., Dere, K.P., Young, P.R., Mason, H.E.: 1999, CHIANTI - an atomic database for emission lines. III. Continuum radiation and extension of the ion database. *Astron. Astrophys. Suppl.* **135**, 339. [DOI](#). [ADS](#).

Lemen, J.R., Title, A.M., Akin, D.J., Boerner, P.F., Chou, C., Drake, J.F., Duncan, D.W., Edwards, C.G., Friedlaender, F.M., Heyman, G.F., Hurlburt, N.E., Katz, N.L., Kushner, G.D., Levay, M., Lindgren, R.W., Mathur, D.P., McFeaters, E.L., Mitchell, S., Rehse, R.A., Schrijver, C.J., Springer, L.A., Stern, R.A., Tarbell, T.D., Wuelsler, J.-P., Wolfson, C.J., Yanari, C., Bookbinder, J.A., Cheimets, P.N., Caldwell, D., Deluca, E.E., Gates, R., Golub, L., Park, S., Podgorski, W.A., Bush, R.I., Scherrer, P.H., Gummin, M.A., Smith, P., Auker, G., Jerram, P., Pool, P., Soufli, R., Windt, D.L., Beardsley, S., Clapp, M., Lang, J., Waltham, N.: 2012, The Atmospheric Imaging Assembly (AIA) on the Solar Dynamics Observatory (SDO). *Sol. Phys.* **275**, 17. [DOI](#). [ADS](#).

Lindsey, C., Braun, D.C.: 2000, Basic Principles of Solar Acoustic Holography - (Invited Review). *Sol. Phys.* **192**, 261. [DOI](#). [ADS](#).

Markwardt, C.B.: 2009, Non-linear Least-squares Fitting in IDL with MPFIT. In: Bohlender, D.A., Durand, D., Dowler, P. (eds.) *Astronomical Data Analysis Software and Systems XVIII, Astronomical Society of the Pacific Conference Series* **411**, 251. [DOI](#). [ADS](#).

Mazzotta, P., Mazzitelli, G., Colafrancesco, S., Vittorio, N.: 1998, Ionization balance for optically thin plasmas: Rate coefficients for all atoms and ions of the elements H to NI. *Astron. Astrophys. Suppl.* **133**, 403. [DOI](#). [ADS](#).

Moreton, G.E., Ramsey, H.E.: 1960, Recent Observations of Dynamical Phenomena Associated with Solar Flares. *Publ. Astron. Soc. Pac.* **72**, 357. [DOI](#). [ADS](#).

Moses, D., Clette, F., Delaboudinière, J.-P., Artzner, G.E., Bouquet, M., Brunaud, J., Carabetian, C., Gabriel, A.H., Hochdezel, J.F., Millier, F., Song, X.Y., Au, B., Dere, K.P., Howard, R.A., Kreplin, R., Michels, D.J., Defise, J.M., Jamar, C., Rochus, P., Chauvineau, J.P., Marioge, J.P., Catura, R.C., Lemen, J.R., Shing, L., Stern, R.A., Gurman, J.B., Neupert, W.M., Newmark, J., Thompson, B., Maucherat, A., Portier-Fozzani, F., Berghmans,

D., Cugnon, P., Van Dessel, E.L., Gabryl, J.R.: 1997, EIT Observations of the Extreme Ultraviolet Sun. *Sol. Phys.* **175**, 571. [DOI](#). [ADS](#).

Nitta, N.V., Schrijver, C.J., Title, A.M., Liu, W.: 2013, Large-scale Coronal Propagating Fronts in Solar Eruptions as Observed by the Atmospheric Imaging Assembly on Board the Solar Dynamics Observatory—an Ensemble Study. *Astrophys. J.* **776**, 58. [DOI](#). [ADS](#).

Nitta, N.V., Liu, W., Gopalswamy, N., Yashiro, S.: 2014, The Relation Between Large-Scale Coronal Propagating Fronts and Type II Radio Bursts. *Sol. Phys.* **289**, 4589. [DOI](#). [ADS](#).

Patsourakos, S., Vourlidas, A.: 2009, "Extreme Ultraviolet Waves" are Waves: First Quadrature Observations of an Extreme Ultraviolet Wave from STEREO. *Astrophys. J. Lett.* **700**, L182. [DOI](#). [ADS](#).

Reid, H.A.S., Ratcliffe, H.: 2014, A review of solar type III radio bursts. *Research in Astronomy and Astrophysics* **14**, 773. [DOI](#).

Sadykov, V.M., Stefan, J.T., Kosovichev, A.G., Stejko, A.M., Kowalski, A.F., Allred, J.C., Kerr, G.S.: 2024, Can Proton Beam Heating Flare Models Explain Sunquakes? *Astrophys. J.* **960**, 80. [DOI](#). [ADS](#).

Scherrer, P.H., Schou, J., Bush, R.I., Kosovichev, A.G., Bogart, R.S., Hoeksema, J.T., Liu, Y., Duvall, T.L., Zhao, J., Title, A.M., Schrijver, C.J., Tarbell, T.D., Tomczyk, S.: 2012, The Helioseismic and Magnetic Imager (HMI) Investigation for the Solar Dynamics Observatory (SDO). *Sol. Phys.* **275**, 207. [DOI](#). [ADS](#).

Sharykin, I.N., Kosovichev, A.G.: 2020, Sunquakes of Solar Cycle 24. *Astrophys. J.* **895**, 76. [DOI](#). [ADS](#).

Stefan, J.T., Kosovichev, A.G.: 2020, Estimation of Key Sunquake Parameters through Hydrodynamic Modeling and Cross-correlation Analysis. *Astrophys. J.* **895**, 65. [DOI](#). [ADS](#).

Stefan, J., Kosovichev, A.: 2025, An Acoustic Model for Sunquakes Unifying the Solar Interior and Atmosphere. *arXiv e-prints*, arXiv:2509.06848. [DOI](#). [ADS](#).

Tan, B., Chen, F., Zhang, Y., Tan, C., Huang, J., Yan, Y.: 2023, Drifting quasi-periodic pulsations of solar microwave bursts and their physical origin. *Advances in Space Research* **71**, 684. [DOI](#).

The SunPy Community, Barnes, W.T., Bobra, M.G., Christe, S.D., Freij, N., Hayes, L.A., Ireland, J., Mumford, S., Perez-Suarez, D., Ryan, D.F., Shih, A.Y., Chanda, P., Glogowski, K., Hewett, R., Huggett, V.K., Hill, A., Hiware, K., Inglis, A., Kirk, M.S.F., Konge, S., Mason, J.P., Maloney, S.A., Murray, S.A., Panda, A., Park, J., Pereira, T.M.D., Reardon, K., Savage, S., Sipócz, B.M., Stansby, D., Jain, Y., Taylor, G., Yadav, T., Rajul, Dang, T.K.: 2020, The SunPy Project: Open Source Development and Status of the Version 1.0 Core Package. *The Astrophysical Journal* **890**. [DOI](#). [URL](#).

Thomas, R.J., Starr, R., Crannell, C.J.: 1985, Expressions to Determine Temperatures and Emission Measures for Solar X-Ray Events from GOES Measurements. *Sol. Phys.* **95**, 323. [DOI](#). [ADS](#).

Thompson, B.J., Plunkett, S.P., Gurman, J.B., Newmark, J.S., St. Cyr, O.C., Michels, D.J.: 1998, SOHO/EIT observations of an Earth-directed coronal mass ejection on May 12, 1997. *Geophys. Res. Lett.* **25**, 2465. [DOI](#). [ADS](#).

Uchida, Y.: 1968, Propagation of Hydromagnetic Disturbances in the Solar Corona and Moreton's Wave Phenomenon. *Sol. Phys.* **4**, 30. [DOI](#). [ADS](#).

Verbeeck, C., Kraaijkamp, E., Ryan, D.F., Podladchikova, O.: 2019, Solar Flare Distributions: Lognormal Instead of Power Law? *Astrophys. J.* **884**, 50. [DOI](#). [ADS](#).

Vršnak, B., Warmuth, A., Temmer, M., Veronig, A., Magdalenić, J., Hillaris, A., Karlický, M.: 2006, Multi-wavelength study of coronal waves associated with the CME-flare event of 3 November 2003. *Astron. Astrophys.* **448**, 739. [DOI](#). [ADS](#).

Warmuth, A., Vršnak, B., Aurass, H., Hanslmeier, A.: 2001, Evolution of Two EIT/H α Moreton Waves. *Astrophys. J. Lett.* **560**, L105. [DOI](#). [ADS](#).

Warmuth, A., Vršnak, B., Magdalenić, J., Hanslmeier, A., Otruba, W.: 2004, A multiwavelength study of solar flare waves. I. Observations and basic properties. *Astron. Astrophys.* **418**, 1101. [DOI](#). [ADS](#).

White, S.M., Thomas, R.J., Schwartz, R.A.: 2005, Updated Expressions for Determining Temperatures and Emission Measures from GOES Soft X-Ray Measurements. *Sol. Phys.* **227**, 231. [DOI](#). [ADS](#).